Investigating the Impact of Nanoparticle Size on Active and Passive Tumor Targeting Efficiency

Edward A. Sykes,[†] Juan Chen,[#] Gang Zheng,[∥,#] and Warren C.W. Chan[†,‡,§,¶,⊥,*]

[†]Institute of Biomaterials and Biomedical Engineering, [‡]Donnelly Centre for Cellular and Biomolecular Research, [§]Department of Chemical Engineering, [¶]Department of Chemistry, [⊥]Department of Material Science and Engineering, and [∥]Department of Medical Biophysics, University of Toronto, Toronto, Canada M5S 3G9 and [#]Ontario Cancer Institute, University Health Network, Toronto, Canada M5T 2M9

ABSTRACT Understanding the principles governing the design of nanoparticles for tumor targeting is essential for the effective diagnosis and treatment of solid tumors. There is currently a poor understanding of how to rationally engineer nanoparticles for tumor targeting. Here, we engineered different-sized spherical gold nanoparticles to discern the effect of particle diameter on passive (poly(ethylene glycol)-coated) and active (transferrin-coated) targeting of MDA-MB-435 orthotopic tumor xenografts. Tumor accumulation of actively targeted nanoparticles was found to be 5 times faster and approximately 2-fold higher relative to their passive counterparts within the 60 nm diameter range. For 15, 30, and 100 nm, we observed no significant differences. We hypothesize that such enhancements are the result of an increased capacity to penetrate into tumors and preferentially associate with cancer cells. We also use computational modeling to explore the mechanistic parameters that can impact tumor accumulation efficacy. We demonstrate that tumor accumulation can be mediated by high nanoparticle avidity and are weakly dependent on their plasma clearance rate. Such findings suggest that empirical models can be used to rapidly screen novel nanomaterials for relative differences in tumor targeting without the need for animal work. Although our findings are specific to MDA-MB-435 tumor xenografts, our experimental and computational findings help to enrich knowledge of design considerations that will aid in the optimal engineering of spherical gold nanoparticles for cancer applications in the future.

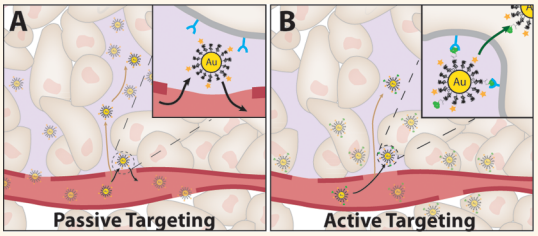

KEYWORDS: gold nanoparticles · tumor targeting · analytical model · surface chemistry · transferrin · nanoparticle design · real-time imaging

Researchers have been heavily focused on the development of novel nanomaterials for the noninvasive detection and treatment of cancer. Unfortunately, efficient tumor targeting[1,2] has been hindered by a poor understanding of how the physical and chemical properties of nanoparticles impact their interactions with biological systems.

There are a number of possible mechanisms for the delivery of nanoparticles into tumors (*e.g.*, vesicle targeting, macrophage delivery). However, the standing mechanism of nanoparticle delivery is through the characteristic leaky blood vessels and compromised lymphatic system of the tumor. Over normal tissues, this abnormal microenvironment is believed to aid in entry and accumulation of nanoparticles *via* passive and active targeting strategies. Passively targeted particles have been shown to nonspecifically enter the tumor based on their size and shape. Inert surface coatings such as poly(ethylene glycol) (PEG) enhance the passive tumor uptake of nanoparticles by preventing serum protein binding and the subsequent plasma clearance by macrophages.[3] This lengthened circulation lifetime is hypothesized to enhance tumor delivery by maintaining a high concentration of nanoparticles in the bloodstream for tumor extravasation. Alternatively, active targeting attempts to enhance the retention and specificity of passive nanoparticle delivery systems by coating their surfaces with antibodies, peptides, and aptamers that recognize and bind to blood vessels, overexpressed cancer cell receptors, and other components of the tumor microenvironment (Figure 1).

There has been much discussion as to whether chemical modification of nanoparticles with targeting ligands can significantly enhance particle delivery to tumors. Previous studies have shown that active

* Address correspondence to warren.chan@utoronto.ca.

Received for review January 16, 2014 and accepted May 12, 2014.

Published online May 12, 2014
10.1021/nn500299p

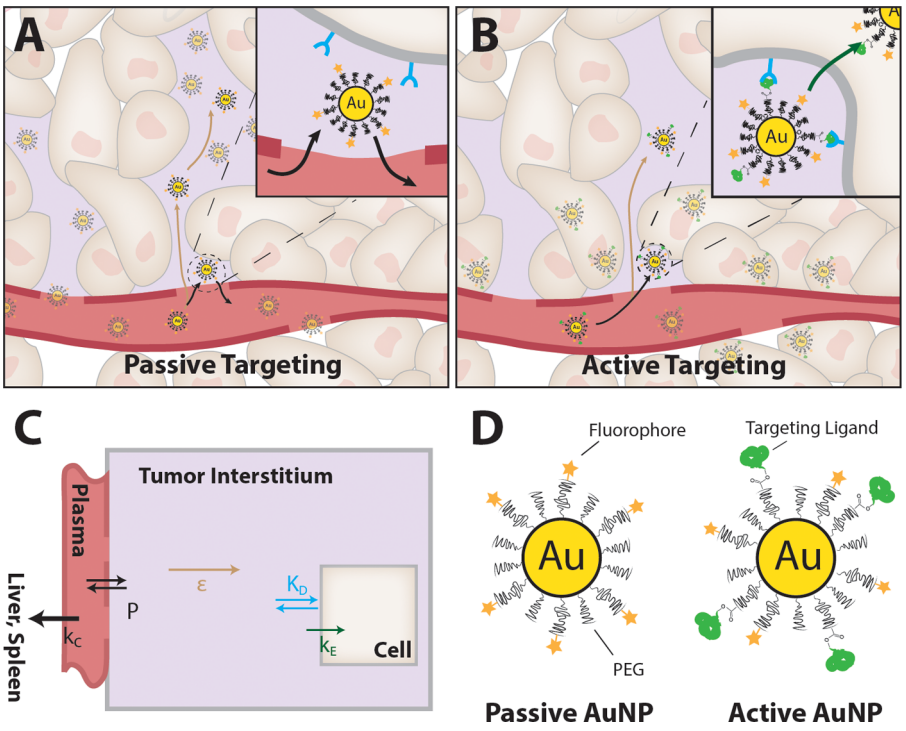

Figure 1. Illustration of the proposed mechanism for passive (A) and active (B) gold nanoparticle tumor targeting exploited in this study. Systemically circulating nanoparticles enter the tumor space through leaky blood vessels and may sequester in cancer cells (beige) or in vascular pools (purple) of the interstitial matrix. Insets demonstrate that passive particles do not directly associate with cancer cells, while active particles are capable of endocytosis through surface-bound targeting ligands (green). Actively targeted particles can also be designed to target the tumor vasculature but are not explored in this study. (C) Graphical representation of a computational model adapted from the Wittrup group[36] that predicts tumor delivery of nanoparticles. Nanoparticle uptake and retention depends on their blood clearance rate (k_C) *versus* their blood vessel permeability (P), fraction of volume available for diffusion (ε), tumor cell dissociation constant (K_D), and internalization rate (k_E). (D) Model nanoparticle designs used in this study.

targeting schemes can improve tumor delivery[4,5] for some nanoparticle formulations while providing minimal benefit over nontargeted approaches for other designs.[6−8] However, only a limited number of designs have been used to evaluate active and passive targeting strategies. The size, shape, and surface chemistry have been demonstrated to mediate cellular uptake,[9−11] macrophage clearance,[12] and biodistribution[13−16] of nanomaterials. Accordingly, differences in nanoparticle design are a likely contributor to the inconsistent conclusions pertaining to active tumor targeting efficacy. Here, we systematically study the role of spherical nanoparticle size in mediating passive and active tumor targeting in an attempt to bridge the disparities in current knowledge. We also demonstrate that computational modeling can be used to simulate our results. Though further work on different nanoparticle designs (shape and surface chemistry) and tumor types is necessary, the outcome of this study will help to enhance the design of spherical nanoparticles for tumor targeting and presents a mathematical method to rapidly screen novel particle designs without the need of animal models.

RESULTS AND DISCUSSION

Nanoparticle Design and Characterization. Gold nanoparticles (AuNPs) were chosen in this study for their broad use in nanomedical research. AuNPs can be easily and stably surface-modified *via* thiol-metal chemistry. They are also biologically inert, nontoxic and can be accurately synthesized with different shapes and sizes ranging from 3 to 200 nm. AuNPs with core diameters of 15, 30, 60, and 100 nm were prepared for passive and active targeting by surface modification with either PEG or PEG in conjunction to OPSS-modified transferrin (Figure 2). The addition of surface ligands increased AuNP hydrodynamic diameters (HD) by ~30−60 nm. Successful surface modification of particles was confirmed by agarose gel electrophoresis (Figure S1). Fluorescent labeling of all formulations was achieved using a method developed by Chou *et al.*,[17] where the fluorescent PEG length was tuned to minimize fluorescent quenching caused by the gold core (Figure S2). Transferrin and fluorescent PEG quantities on particle surfaces were empirically chosen to ensure optimal fluorescence. AuNPs were also tuned by mPEG blocking to ensure particle zeta-potentials were within the neutral range so as to minimize charge-specific differences in cell and tumor uptake that have been reported previously for positively and negatively charged particles.[18] Fluorescent PEG on active and passive formulations was held constant, while transferrin density was maintained between 0.02 and

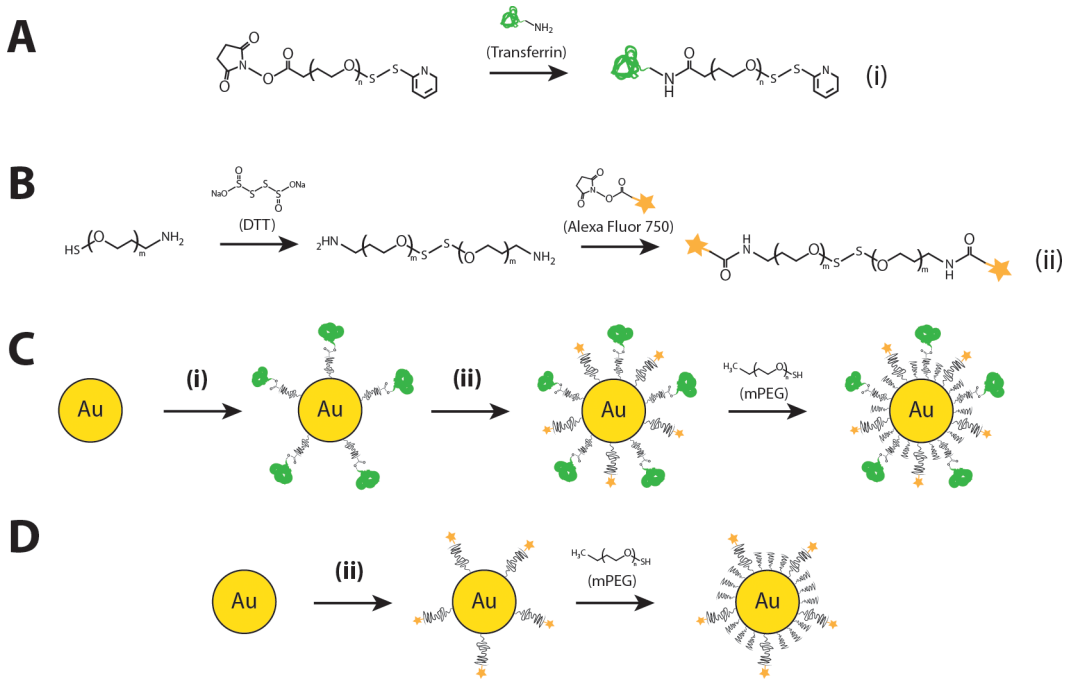

Figure 2. Images depicting the chemical synthesis of PEG components and functionalization of nanoparticles. (A,B) Process of conjugating OPSS-PEG to transferrin (green) and the labeling of Alexa Fluor 750 (yellow) to nPEG. (C,D) Gold nanoparticles surface-modified to create actively and passively targeted particles in this study. Representative image of OPSS-PEG-transferrin conjugates. True degree of OPSS-PEG labeling of transferrin in (i) was calculated to be 2.5. Schematics are not to scale.

0.04 ligands/nm^2 for all active AuNPs to ensure that differences in tumor targeting were related to targeting modality and size over differences in ligand density. Table 1 provides a summary of the functionalized AuNPs used in this study.

The effect of serum proteins on our active and passive AuNPs was studied to ensure that serum-induced changes to AuNP surface chemistry were minimal. Particles were incubated with serum and monitored for the release of surface ligands over 48 h. We confirmed that AuNP-bound A750-PEG was resistant to desorption for the period of study (Figure S3). Further, the adsorbed serum protein profiles for AuNPs (Figure S1C) showed that (i) opsonization was low for both active and passive designs compared to bare particles[12] and (ii) the presence of transferrin on actively targeted particle surfaces was conserved. Together, these results indicate that the surfaces of our AuNPs were sufficiently passivated to prevent alterations by the biological environment[12] and verified that our results were unconfounded by the influence of ligand desorption or adsorbed serum protein corona.[12,19,20] The targeting property for active and passive schemes was also confirmed *in vitro* by cell binding analysis using inductively coupled plasma atomic emission spectroscopy. Cellular uptake of actively targeted particles was consistently higher than passive formulations but could be competitively reversed by the addition of free transferrin to cell media (Figure S4). Larger particles were also found to achieve stronger affinity to cancer cells than their smaller counterparts[9,21] (Figure S5 and Table 1). The confirmed specificity of actively targeted AuNPs for transferrin receptor in the presence of serum indicated that the OPSS-PEG spacer prevented loss of targeting function by distancing transferrin from the adsorbed serum protein brush layer.[22,23]

TABLE 1. Characteristics of Active and Passive AuNPs Used in This Study

AuNP (nm)	design	HD[a] (nm)	TF (#/AuNP)	ZP[b] (mV)	K_D[c] (nM)	k_c[d] (h^{-1})
15	passive	46.3 ± 0.1	N/A	−6.7 ± 6	10[e]	0.069
	active	49.5 ± 0.1	7.3 ± 0.3	−0.64 ± 7	3.7×10^{-3}	0.142
30	passive	64.2 ± 0.1	N/A	−15 ± 8	10[e]	0.087
	active	60.0 ± 0.1	17.2 ± 0.6	−11 ± 11	6.9×10^{-4}	0.135
60	passive	104.2 ± 0.2	N/A	−10 ± 4	10[e]	0.090
	active	100.4 ± 0.1	27.3 ± 0.8	−9 ± 4	7.6×10^{-5}	0.176
100	passive	166.0 ± 0.1	N/A	−6 ± 4	10[e]	0.233
	active	175.6 ± 0.1	80 ± 4	−5 ± 5	2.0×10^{-6}	0.245

[a]Hydrodynamic diameter (HD). Error denotes polydispersity index. [b]Zeta-potential (ZP) as measured by dynamic light scattering. [c]Calculated dissociation constant between AuNP and tumor cells. [d]AuNP blood clearance rates. [e]Value assumed to be similar to isotype antibody (nonspecific association to cellular target).

Justification and Validation of AuNP Tracking Using Fluorescence. To determine the accuracy of the measurements, it was important to ensure that our analytical technique was appropriate for the real-time assessment of systemic delivery of AuNPs to tumors. Fluorescence was chosen as our mode of analysis as it is a nondestructive technique that can minimize discrepancies associated with mouse-to-mouse variability by allowing AuNPs to be tracked within the same animal

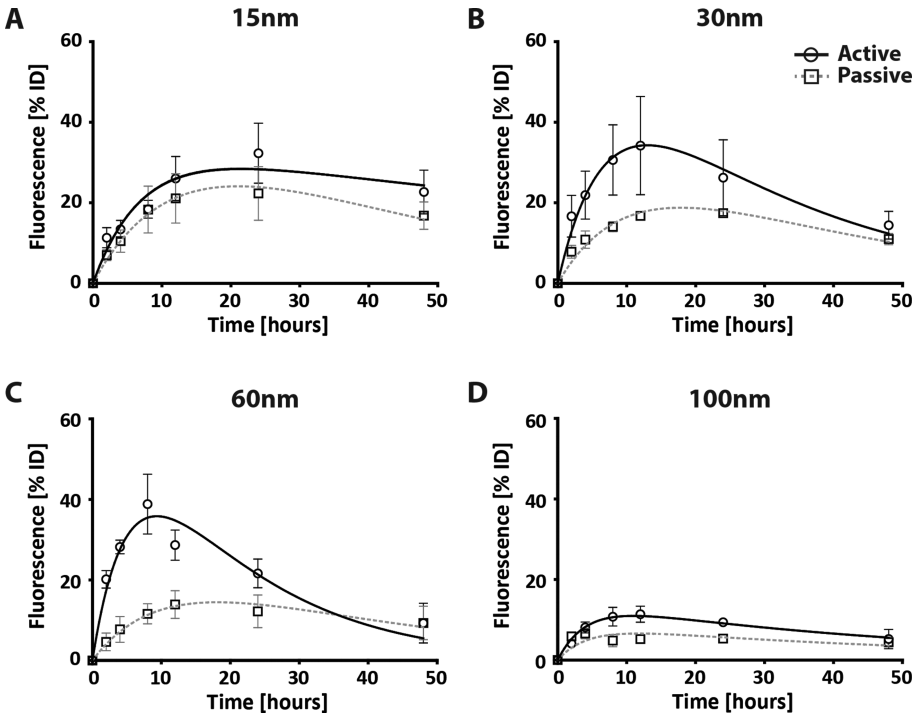

Figure 3. Kinetic profiles ($n > 3$) depicting the relative tumor fluorescence for mice injected with passive (dotted) and active (solid) AuNPs over 48 HPI. Graphs A−D illustrate tumor uptake of 15−100 nm diameter AuNPs, respectively. Tumor fluorescence (% ID) denotes the relative difference in tumor signal to opposing mouse flank expressed as a percentage of tumor fluorescence immediately after injection. Error bars represent the standard error mean values for each time point.

over time. Although fluorescence is not an absolute measure of nanoparticles, it was useful for the head-to-head comparisons of the relative differences in tumor delivery of active and passive AuNPs. We assessed the impact of tissue depth on tracking of AuNP fluorescence *in vivo* using tissue phantoms[24] composed of agarose−mouse homogenate hydrogels of varying thicknesses (1−8 mm). Nanoparticle fluorescence was demonstrated to decay predictably with tissue depth for all AuNP concentrations (Figure S6). This showed that imaging depth would not influence our relative comparisons of fluorescence between designs.

CD1 nude athymic mice with orthotopic unilateral human MDA-MB-435 tumor xenografts were used in our studies to compare active and passive tumor targeting using fluorescence. Overexpression of transferrin receptors (CD71) in our MDA-MB-435 tumor model[25] was assessed by flow cytometry and immunofluorescent histology. CD71 expression was confirmed and was found to be higher than our nonmalignant tissue control (Figure S7). This validated that active targeting through transferrin was suitable for specific targeting of our tumor model. Injection doses for each particle design were adjusted to achieve a total AuNP surface area of 70.6 cm^2 and monitored in mice by real-time fluorescence imaging at 0−48 h postinjection (HPI). Representative images of bulk AuNP distribution in tumor-bearing mice can be found in Supporting Information Figure S8. Total fluorescence intensity of the tumor and opposing mouse flank were measured at each time point and processed with ImageJ according to previously published methods[17] to calculate the relative tumor accumulation of AuNPs. Briefly, tumor and flank fluorescence was normalized to their respective intensities at 0 HPI (Figure S9). As seen in Figure 3, differences in targeting scheme and particle size mediated tumor delivery of AuNPs in a manner distinct from freely injected fluorescent PEG (Figure S10).

Effect of Size on Tumor Accumulation of Active and Passive AuNPs. Area under the curve (AUC) was calculated from the fluorescent profiles presented in Figure 3 and 4a to compare the relative differences in tumor accumulation for each AuNP design. Similar to previously reported findings,[16] smaller AuNPs achieved higher AUC values than larger formulations for both active and passive targeting schemes (Figure 4B). We hypothesized that the enhanced tumor accumulation of small AuNPs was related to an extension of time available for AuNPs to extravasate into tumors resulting from slower plasma clearance (Table 1). AUC values for actively targeted AuNPs trended higher than their passively targeted counterparts for diameters between 15 and 60 nm. However, active accumulation was only statistically higher than passive delivery for 60 nm AuNPs (student's t test $p < 0.1$). The 60 nm transferrin-coated AuNPs exhibited 1.9 times higher tumor accumulation compared to passive designs ($p < 0.1$). This suggested that, for our tumor model, enhancements in delivery provided by active targeting were only effective in the finite size range of 60 nm. The enhanced utility of active

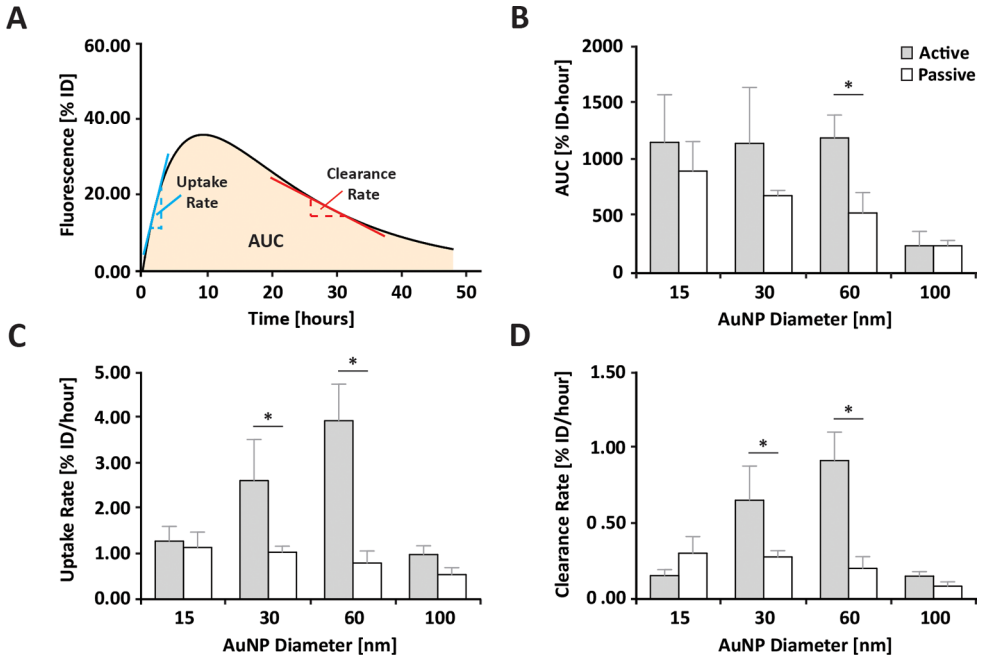

Figure 4. Graphs depicting AuNP uptake by tumors. (A) Graphical summary of how tumor delivery parameters were calculated from the regression fits found in Figure 3. (B) Comparison of the relative tumor accumulation (AUC) at 48 HPI for each formulation. (C,D) Calculated AuNP−tumor uptake and clearance rates, respectively. Error bars represent standard error of the mean ($n > 3$); * indicates pairs that were statistically different ($p < 0.1$); % ID denotes tumor fluorescence expressed as the percentage of tumor fluorescence immediately after injection.

targeting in the 60 nm range was attributed to their cellular interactions. As previously shown, smaller AuNPs are less likely to remain in tumors as they are thermodynamically less favorable for receptor-mediated endocytosis and exhibit an enhanced propensity for exocytosis[26−28] than targeted formulations within the 40−60 nm range.[29] As a result, smaller particles may be forced out of the tumor due to high interstitial pressures.[30,31]

Our results reinforce the importance of AuNP diameter in modulating active tumor targeting. Specifically, they illustrate that particles in the 15 nm range may be too small to be mediated by active targeting while diameters exceeding 100 nm may be cleared from the blood too quickly for sufficient tumor delivery. The unique enhancement of active targeting character of 60 nm particles is of particular interest as it provides a rationale for the enhanced therapeutic function of actively targeted nanomaterials in the absence of increased tumor accumulation presented by other groups, by illustrating that the contrasting findings may be related to the specific particle sizes used in each study.[6,7,32]

Evaluation of the Rate of AuNP Transport into and out of Tumors. The rates of tumor entry (k_{in}) and exit (k_{out}) for passive and active nanoparticle designs were calculated by taking the average slopes of tumor accumulation and clearance from the fluorescence profiles seen in Figure 3. Passive designs achieved k_{in} and k_{out} values ranging from 0.54 to 1.15% ID/h and 0.09−0.30% ID/h, while active AuNPs were found to be 1.00−3.94 and 0.15−0.92% ID/h, respectively.

As seen in Figure 4, tumor accumulation of actively targeted 30 and 60 nm particles were 2 and 5 times faster than their passive counterparts but were also cleared 2 and 4 times faster, respectively (student's t test, $p < 0.1$). These findings along with our AUC results insinuate that active targeting can enhance the speed of AuNP delivery to MDA-MB-435 tumors in spite of their faster tumor clearance. Although the mechanism is unclear, this would indicate that, for spherical AuNPs, the rate of tumor uptake may be the dominating mediator for tumor accumulation.

Examination of AuNP Penetration into Tumor Tissues. The effect of AuNP design on tissue penetration depth was studied *via* histopathology of tumor sections harvested 48 HPI. Sections were stained with silver, CD31 antibodies, and hemotoxylin−eosin to visualize AuNPs, blood vessels, and tumor tissue features, respectively. Densitometry profiles were developed using a custom ImageJ macro and fit to a standard model of analyte diffusion (eq 1) to calculate AuNP diffusivity (D), where C denotes AuNP intensity, r represents the AuNP diffusion distance, and t indicates the time of analysis postinjection.[33]

$$C(r,t) = \frac{1}{2}\left[\mathrm{erfc}\left(\frac{r}{2\sqrt{Dt}}\right)\right] \quad (1)$$

Similar to previous work, both size and surface chemistry affected tumor penetration.[16,34] Small passively targeted AuNPs diffused further into the tumor microenvironment than larger sizes (Figure 5),

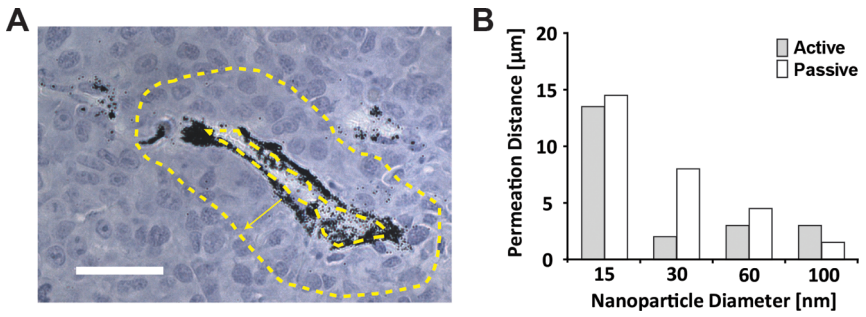

Figure 5. Tumor tissue penetration of AuNPs at 48 HPI. (A) Diagram of AuNPs (dark black) distribution away from tumor blood vessels was calculated. Yellow dotted outline illustrates the region of interest expanding radially from a tumor blood vessel. Bar graph in (B) summarizes the permeation distances where AuNPs reach 20% of blood vessel intensity. Scale bar denotes 25 μm. Error bars in (B) represent standard deviation values. Error bars are not visible due to magnitude.

while actively targeted particles with diameters between 30 and 60 nm penetrated 77−85% less than passive designs (Figure 5B). The proximity of a nanoparticle to blood vessels is believed to dictate its retention within the tumor space[2,16] as particles neighboring blood vessels are more likely to return to the bloodstream than deeper diffusing species. In agreement with this theory, the tumor retention of our passive AuNPs exhibited less favorable tissue penetration.

In contrast, tumor accumulation of active AuNPs was higher in spite of their reduced tumor diffusivity. This implies that surface modification of spherical AuNPs for association with cancer cells may aid in tumor retention. As mentioned previously, the cellular uptake of active AuNPs is optimal in the 60 nm range,[26,27] while 15 nm AuNPs are rapidly exocytosed.[16] Taken with the limited tumor permeation of 100 nm AuNPs,[35] these observations infer that spherical 60 nm active AuNPs can exploit both tissue penetration and cancer cell interaction *in vivo* for enhanced delivery to MDA-MB-435 tumors.

Computational Modeling as a Tool for AuNP Screening. The above work demonstrates that the design of AuNPs for efficient tumor delivery is nontrivial. The countless permutations of nanoparticle designs render the examination of every physicochemical parameter for tumor delivery infeasible. Computational techniques can potentially reduce experimental work by rapidly screening new nanoparticle formulations. An analytical model developed by the Wittrup group[36] (Figure 1C) was applied as a proof-of-concept technique to predict tumor delivery efficiency of different spherical AuNPs using our experimental data.

Constraints of the Wittrup model, described by eqs 2 and 3, were satisfied by assuming (i) the extravasation of AuNPs was the rate-limiting step in total tumor accumulation and (ii) AuNPs internalized by cancer cells were subject to endocytic degradation. Although our data does not provide evidence that cellular internalization can cause degradation of AuNPs, this phenomenon has been reported for other inorganic nanoparticles.[37] In addition, this assumption accounts for modification of nanoparticle surface chemistry and metabolism of polymeric particles caused by cellular uptake.[38,39]

TABLE 2. Fitted Results of Experimental Data for AuNP Delivery to Tumors

AuNP (nm)	design	P (μm/h)	k_E (h^{-1})	ε	X^2	R^2
15	passive	41.92	0.024	0.262	0.02	0.99
	active	62.64	0.008		0.16	0.93
30	passive	38.74	0.026	0.163	0.48	0.95
	active	92.33	0.043		0.05	0.93
60	passive	29.13	0.024	0.111	0.04	0.96
	active	142.14	0.059		0.32	0.93
100	passive	24.79	0.013	0.057	1.22	0.41
	active	43.89	0.021		0.05	0.98

$$\mathrm{AuNP_{tumor}} = \left(\frac{2PR_{cap}}{R_k^2}\right)\left(\frac{\mathrm{AuNP_{initial}}(e^{-k_c t} - e^{-\Omega t})}{\Omega - k_c}\right) \quad (2)$$

$$\Omega = \left(\frac{2PR_{cap}}{\varepsilon R_k^2}\right)\left(\frac{K_D}{\frac{[Ag]}{\varepsilon} + K_D}\right) + k_E\left(\frac{\frac{[Ag]}{\varepsilon}}{\frac{[Ag]}{\varepsilon} + K_D}\right) \quad (3)$$

Model parameters were obtained from literature or experimentally measured *in vitro* wherever possible, while the internalization rate constant (k_E) was calculated by nonlinear regression using the plots presented in Figure 3. The regression-fitted parameters for each AuNP design are summarized in Tables 2 and 3. A comparison between experimentally derived measurements of tumor accumulation of AuNPs *versus* simulated AUC values (Figure S11) confirmed that the fitted model accurately predicted the accumulation characteristics of the particle designs used in our study.

Using this model construct, we simulated the impact of effective cancer cell affinity (K_D) and plasma clearance rate (k_C) on the relative changes in AuNP

TABLE 3. Definition of Model Parameters

symbol	description	location	source
D	diffusion coefficient in tumor ($\mu m^2/h$)	Table 4	measured
D_{free}	diffusion coefficient in solution ($\mu m^2/h$)	Supporting Information	calculated
D_{pore}	diffusion coefficient in cylindrical pore ($\mu m^2/h$)	Supporting Information	calculated
K_D	dissociation constant (k_{off}/k_{on}) (M)	Table 1	measured
k_C	AuNP plasma clearance rate (h^{-1})	Table 1	measured
k_E	cell internalization rate (h^{-1})	Table 2	fitted
R_{cap}	capillary radius (μm)	8	ref 45
R_k	intercapillary distance (μm)	102	measured
P	tumor capillary permeability ($\mu m/h$)	Table 2	fitted
R_{pore}	radius of interstitial pore (nm)	500	ref 36
ψ	partition coefficient in pore	Supporting Information	calculated
[Ag]	CD71 concentration in tumor (M)	7.0×10^{-8}	calculated/ref 46
$[AuNP]_{initial}$	initial relative plasma fluorescence of AuNPs (% ID/mL)	50	ref 36
$[AuNP]_{tumor}$	relative fluorescence of AuNP in tumor (% ID/mL)	Figure 2	fitted
ε	available volume fraction of the tumor interstitium	Table 2	calculated

TABLE 4. Summary of Calculated AuNP Diffusivity ($\mu m^2/h$) in Tumors

	actively targeted	passively targeted
15 nm	14.17 ± 0.03	22.28 ± 0.03
30 nm	3.91 ± 0.01	49.87 ± 0.01
60 nm	10.1 ± 0.02	45.13 ± 0.01
100 nm	3.88 ± 0.01	0.25 ± 0.01

accumulation within the tumor (AUC). These parameters (K_D and k_C) were chosen as they are tunable *via* changes to particle size and surface chemistry that can be easily characterized *in vitro*. As shown in Figure 6, the heat maps predicted that variations in K_D or k_C resulted in similar changes to AUC for all AuNP designs. AUC values for spherical nanoparticles were not augmented by lengthening plasma half-lives beyond 3 h for either targeting scheme. Our simulations also suggested that the enhancements associated with active targeting only became apparent for AuNPs with K_D values below 10^{-12} M. The predicted impact of blood half-life corresponds with published data that show that tumor uptake for a given size range does not substantially differ when plasma half-lives were extended from 3 to 10 h.[16,40] Similarly, the predicted threshold for AuNP−cell affinity was supported by our experimental results as our 15 nm AuNPs were the only tested formulation whose tumor uptake profiles were visually similar to their passive counterparts and also helps to explain the negligible impact of transferrin targeting seen by Choi *et al.* as their reported cell dissociation constants were above our proposed cutoff range.[6]

These findings illustrate that a computational model can be used to rapidly compare new designs and to establish design criteria for optimizing tumor targeting. In light of the differences in permeability, receptor expression, and vascularization of different tumor types as well as the differences in targeting character

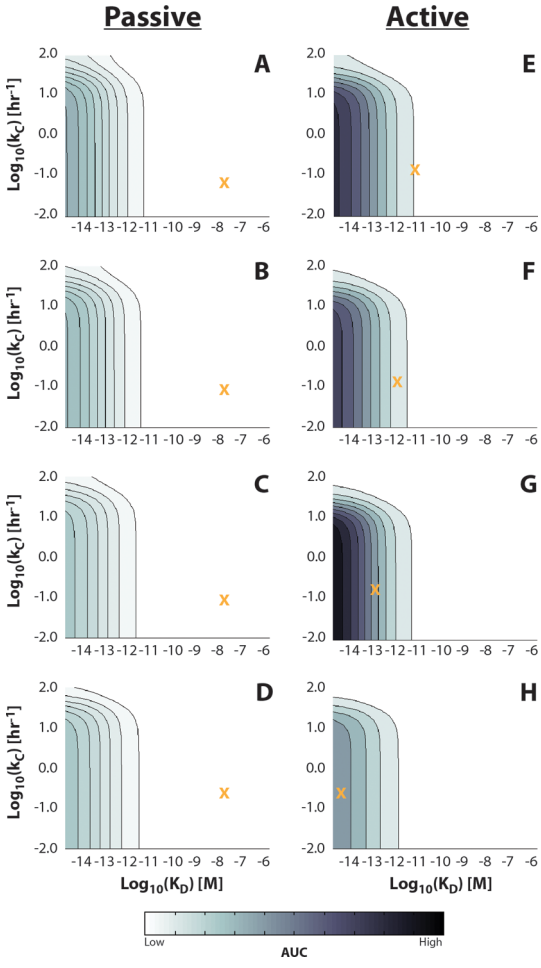

Figure 6. Log-based contour plots depicting the simulated AUC values for AuNPs of 15 (A,E), 30 (B,F), 60 (C,G), and 100 nm (D,H) diameters when k_C and K_D were simultaneously varied. Intensity in the heat maps illustrates AUC in cumulative fluorescent units expressed as the percentage of initial tumor fluorescence (% ID·h). Orange "x" indicates the experimental values for each design examined in this study.

associated with other nanoparticle shapes and surface chemistries, the impact of K_D and k_C may vary and

should be investigated in future studies before absolute generalizations can be made. Nevertheless, at minimum, two significant implications can still be drawn from our results for melanoma-based orthotopic tumors: (i) a minimum tumor cell affinity must be met for active targeting of spherical AuNPs to become beneficial over passive targeting, and (ii) lengthening plasma retention alone does not improve tumor delivery of AuNPs.[2,41]

CONCLUSION

In this study, we systematically compared the effect of nanoparticle size on active and passive tumor targeting using eight spherical AuNP formulations in tumors. Our results have helped to explain some of the countervailing observations reported by other groups by establishing the impact of AuNP size on tumor accumulation kinetics for active and passive targeting strategies. We identified that transferrin-decorated AuNPs within the 60 nm range were capable of faster and higher tumor delivery than passive formulations while PEG-coated designs infiltrated deeper into tumors, but at the expense of slower and lower total tumor delivery. Although these findings are specific to orthotopic melanoma tumors and spherical AuNPs, they illustrate the complexity involved with understanding and manipulating AuNP–tumor delivery dynamics. To mitigate this issue, we also proposed and successfully demonstrated here that utilization of the Wittrup tumor accumulation model can aid in (i) quantitatively comparing the tumor homing efficiency of different AuNP designs and (ii) identifying specific nanoparticle design criteria for enhanced tumor delivery without the need for animal experiments. Although this model is far from complete, it illustrates that the rational design of AuNPs is possible and serves as an excellent starting point for the development of computational strategies to predict the performance of nanoparticles in tumor targeting. To validate the broad applicability of our findings, an evaluation of the effect of nanoparticle targeting in different animal models (*e.g.*, genetically engineered mouse models, orthotopic models), human tumors, and with different nanomaterials will be needed since the tumor physiology and particle–tumor interactions are likely to be different. Nonetheless, the development of a theoretical model in combination with our experimental findings will establish a fundamental research framework that can aid in the engineering of nanostructures for future biomedical applications.

MATERIALS AND METHODS

Materials. All chemical reagents related to nanoparticle synthesis were purchased from Sigma-Aldrich, while all biological, analytical, and labeling materials were purchased from Invitrogen unless otherwise stated. Orthopyridyl disulfide-*co*-*N*-hydroxylsuccinimide-functionalized poly(ethylene glycol) (OPSS-PEG-NHS, 5 kDa) was purchased from Nanocs, and methoxy-terminated PEG-thiol (mPEG, 5 kDa) and amine-terminated PEG-thiol (nPEG, 10 kDa) were purchased from Lysan Bio. CD1 nude athymic mice for *in vivo* experiments were purchased from Charles River Laboratories. Biological extracellular matrix (Matrigel, CB40234) for engraftment of tumor xenografts was purchased BD Biosciences.

Gold Nanoparticle Synthesis. Gold nanoparticles, 15 nm and larger, were synthesized by citrate reduction and hydroquinone-seeded growth, respectively.[42] The 15 nm gold colloids were produced by reducing gold(III) chloride hydrate (23.5 mM) under reflux with sodium citrate tribasic (1 mM) while stirring for 10 min at a volumetric ratio of 0.125. Larger nanoparticles were synthesized by seed-mediated growth through mixing of gold(III) chloride hydrate (25 mM) with 15 nm gold colloids diluted 100× with double distilled water followed by sequential addition of sodium citrate tribasic (15 mM) and hydroquinone (25 mM) under rapid stirring. Gold precursor, sodium citrate tribasic, and hydroquinone were added at a 1:1 volumetric ratio, while the quantity of gold colloid was varied to manipulate nanoparticle size. Representative images of synthesized designs can be found in Figure S1.

Conjugation of Transferrin to OPSS-PEG-NHS. PEG modification of holo-transferrin was achieved through reaction of holo-transferrin with a 162× molar excess of OPSS-PEG-NHS in sodium bicarbonate buffer (0.1 M, pH 8.5). Conjugation was allowed to complete overnight at 4 °C and was sequentially purified from unreacted components by dialysis (Thermo-Pierce Scientific), gel filtration (G25 Sephadex), and Amicon concentration (Millipore). Conjugation was confirmed by SDS-PAGE electrophoresis (Figure S12) where protein staining (Coomassie stain) was colocalized with the presence of PEG (barium iodide)[43] as well as size-exclusion high-pressure liquid chromatography (HPLC) in a mobile phase of HPLC-grade water (Figure S13). Degree of PEG labeling was determined to be 2.5 PEG/transferrin by Bradford assay and barium iodide staining for protein and PEG quantitation,[44] respectively (Figure S14). Transferrin conjugates were stored at −20 °C prior to use.

Fluorescent Labeling of PEG. Amine-modified PEG-thiol (nPEG) was fluorescently labeled with Alexa Fluor 750 (Invitrogen, A20111) by standard carbodiimide chemistry (Figure 2B). Double distilled water-solubilized nPEG-SH (100 mg/mL) was oxidized using a 1000× molar excess of sodium tetrathionate for 1 h. Postoxidation, solution was dialyzed to remove sodium tetrathionate and concentrated using Amicon ultracentrifugation tubes (Millipore). nPEG was then diluted to a final concentration of 100 mg/mL with 0.1 M sodium bicarbonate (pH 8.5). A 20× molar excess of Alexa Fluor 750 was reacted with the nPEG solution at 4 °C overnight and purified *via* gel filtration using a NAP5 column (GE Scientific). Fluorescent PEG conjugates were confirmed by HPLC (Figure S15).

Gold Nanoparticle Functionalization. Synthesized particles were surface-modified to achieve either active or passive tumor targeting character. As-synthesized particles were washed in double distilled water supplemented with 0.01 wt %/v Tween 20 *via* centrifugation to remove excess citrate and/or hydroquinone prior to surface modification. Actively targeted particles were created by first incubating AuNPs with PEGylated transferrin for 15 min at 60 °C followed by addition of fluorescently labeled PEG for an additional 15 min at 60 °C. To block the remaining surface, methoxyl-PEG-thiol (mPEG) was added and left to bind overnight at 4 °C. Passively targeted formulations were obtained using the same procedure as that of active designs but in the absence of transferrin. The ratio of reacting fluorescently labeled PEG to mPEG was maintained at 1:4 mol/mol at a reaction condition of 4 PEG/nm^2 for all particle designs. The 10 kDa fluorescent PEG was selected over 5 or 1 kDa conjugates as it produced the optimal fluorescent yield when bound to particles (Figure S2). Functionalized particles

were washed in 1× phosphate buffered saline and left concentrated in the refrigerator until use.

Validation of AuNP Designs. Active and passive gold nanoparticles were validated for size, surface charge, and transferrin density (Figure S1). Core diameters were measured using a FEI Tecnai 20 transmission electron microscope, while hydrodynamic diameter and zeta-potentials were determined with a Malvern Zetasizer Nano. Surface density of transferrin was calculated by depletion assay. Effect of serum protein adsorption to particle designs was profiled by SDS-PAGE. Fluorescent PEG stability on surface of nanoparticles was confirmed by monitoring fluorescent PEG desorption for each formulation in the presence of serum over 48 h (Figure S3). For details please refer to the Supporting Information.

Cell Binding Assay. Specificity of active and passive nanoparticles was confirmed by testing nanoparticle binding to MDA-MB-435 cancer cells. Cells were grown to 80% confluence in RPMI 1640 media supplemented with 10% fetal bovine serum and Penestrep. Nanoparticle formulations were incubated with cells under serum-free conditions (RPMI 1640 + 4% BSA + Penestrep) at physiological temperature and atmosphere (37 °C, 5% CO_2) for 2 h. Following incubation, cells were gently washed with PBS (room temperature) four times and frozen pending analysis by inductively coupled plasma atomic emission spectroscopy. Actively targeted nanoparticle specificity for CD71 was validated by competitive inhibition of nanoparticle binding using free holo-transferrin at a final concentration of 2 mg/mL (Figure S4).

Calculation of Cell Dissociation Constants. MDA-MB-435 cells seeded to 80% were sensitized under serum-free culture media supplemented with 4% BSA for 2 h under physiological conditions, washed with warmed 1× PBS, and fixed using ice-cold methanol for 5 min. Cells were then washed in 1× PBS and blocked with 1× PBS supplemented with 4 wt %/v BSA for 1 h. Blocked cells were incubated with nanoparticle formulations ranging in concentration from 4 pM to 1 fM at 37 °C for 1 h. Supernatants were collected and measured against nanoparticle standards to calculate the number of nanoparticles bound to cells. Measured fluorescence was then fit using Graphpad Prism to obtain cell dissociation constants for each nanoparticle size (Figure S5).

Orthotopic Tumor Induction. MDA-MB-435 cells were expanded in tissue culture flasks under cell culture conditions (37 °C with 5% CO_2). On the day of inoculation, cells were harvested and concentrated to 30 million cells/mL by centrifugation (500*g* for 5 min). Cells were mixed at a 1:1 v/v ratio with matrigel and kept on ice. To inoculate tumors, mice were anesthetized by isofluorane inhalation and subcutaneously injected with 150 μL of the cell−matrigel mixture into the subcutaneous hind flank using a 25 gauge needle.

***In Vitro* Validation of Tissue Absorption of Fluorescence.** Tissue phantoms were produced from a 1:1 mixture of mouse homogenate and 4 wt %/v agarose. Briefly, a slurry of homogenized mice and agarose was mixed under continuous stirring at 70 °C. Then 50−150 μL of the agarose mixture was transferred to 96-well plates to achieve the desired gel thicknesses. Gels were then allowed to set at 4 °C for 30 min. Nanoparticles of desired concentrations were then applied to gels and measured from bottom-up using a Carestream Multispectral MS Fx Pro *in vivo* imager under conditions used in our mouse experiments (10 min exposure with fluorescent excitation and emission of 750 and 830 nm). Well plate fluorescence was then processed with ImageJ to compare relative changes in nanoparticle fluorescence associated with tissue thickness (Figure S6).

***In Vivo* Fluorescent Tracking of Nanoparticles.** Three weeks post-tumor inoculation, mice bearing tumors (1.0−1.2 cm in diameter) were selected for targeting experiments. Nanoparticle formulations (equivalent to a total surface area of 70.6 cm^2) were tail-vein-injected into mice at a volume of 0.15 mL. Animals were rendered unconscious by continuous inhalation of isofluorane-enriched oxygen and fluorescently imaged on their dorsal side using a Carestream Multispectral MS Fx Pro *in vivo* imager configured for continuous image capture for 10 min under fluorescent excitation at 750 nm and emission acquisition at 830 nm. Fluorescent images were taken pre- and postinjection to account for animal autofluorescence and track nanoparticle distribution over time.

Calculation of Nanoparticle Pharmacokinetics. Nanoparticle−tumor uptake was calculated from fluorescent images according to previously published methods.[17] Briefly, mean fluorescence of mouse tumor and non-tumor-bearing flank were obtained by ImageJ and subtracted from background controls. At each time point, mean fluorescence of tumor and flank were then normalized to intensities at 0 h postinjection to remove experimental bias. Nanoparticle accumulation was calculated by subtraction of normalized flank values from mean intensities of the tumor. The calculation procedure has been pictorially illustrated in Figure S9. AuNP pharmacokinetic parameters were calculated by profiling the blood of non-tumor-bearing mice. Briefly, mice were injected with AuNPs at a dose equivalent to 70.6 cm^2 followed by tail vein blood extraction (20 μL) at 2, 4, 6, 9, 24, and 48 HPI. Sample fluorescence was referenced against AuNPs diluted with whole mouse blood to calculate AuNP concentrations. Fluorescence was measured in 384 well clear bottom fluorescent plates with the Carestream *in vivo* imager at 20 min exposure with excitation/emission settings of 750/830 nm. Clearance profiles (Figure S16) were then fit to a one-compartment model (eq 4) to calculate the parameters seen in Table S.1.1.

$$\mathrm{AuNP}_{\mathrm{plasma}}(t) = Ae^{-k_c t} \quad (4)$$

Measurement of Nanoparticle Penetration into Tumors. Tumors were harvested 48 HPI, fixed in formalin, and processed by the Pathology Research Unit at Toronto General Hospital. Histological sections were stained with hemotoxylin and eosin for tissue contrast as well as anti-CD31-HRP antibodies and silver stain (Ted Pella, 15718) to visualize blood vessels and nanoparticles, respectively. Slides were imaged at 20× magnification on a Leica DM2000 microscope coupled with a Leica DFC420 camera. Images were then desaturated to isolate for nanoparticles and analyzed using a custom ImageJ macro to profile particle distribution radiating up to 13 μm away from blood vessels at 0.5 μm intervals. Permeation profiles were fit with eq 2 to calculate nanoparticle diffusivity by nonlinear regression in Matlab. Over 50 blood vessels from different tumors ($n > 3$) were analyzed for each design.

Analytical Model Implementation. The analytical model developed by the Wittrup group[36] was adapted for use in our study using parameters specific to each nanoparticle design. The empirical results of nanoparticle fluorescence were fitted in Matlab by nonlinear regression. A detailed explanation of the parameters and model can be found in the Supporting Information.

Conflict of Interest: The authors declare no competing financial interest.

Acknowledgment. We would like to acknowledge the Pathology Department at Toronto General Hospital for their aid in preparing histological slides. We would also like to thank L. Chou and C. Walkey for their protocols for creating fluorescent AuNPs and visualizing AuNP-adsorbed serum protein profiles. W. C. W. C. and G. Z. would like to acknowledge the Canadian Institute of Health Research (MOP-93532; RMF-111623), Natural Sciences and Engineering Research Council (NETGP35015; RGPIN-288231; CRDPJ424710), Collaborative Health Research Program (10002109), Canadian Foundation for Innovation and Ontario Ministry of Research and Innovation for funding support. E.A.S. would also like to acknowledge NSERC for fellowship.

Supporting Information Available: Details of supporting experimental procedures as well as characterization data for nanoparticles and *in vivo* work. This material is available free of charge *via* the Internet at http://pubs.acs.org.

REFERENCES AND NOTES

1. Lammers, T.; Kiessling, F.; Hennink, W. E.; Storm, G. Drug Targeting to Tumors: Principles, Pitfalls and (pre-) Clinical Progress. *J. Controlled Release* **2011**, *161*, 175–187.
2. Jain, R. K.; Stylianopoulos, T. Delivering Nanomedicine to Solid Tumors. *Nat. Rev. Clin. Oncol.* **2010**, *7*, 653–664.

3. Moghimi, S. M.; Hunter, A. C.; Murray, J. C. Long-Circulating and Target-Specific Nanoparticles: Theory to Practice. *Pharmacol. Rev.* **2001**, *53*, 283–318.
4. Qian, X.; Peng, X.-H.; Ansari, D. O.; Yin-Goen, Q.; Chen, G. Z.; Shin, D. M.; Yang, L.; Young, A. N.; Wang, M. D.; Nie, S. *In Vivo* Tumor Targeting and Spectroscopic Detection with Surface-Enhanced Raman Nanoparticle Tags. *Nat. Biotechnol.* **2008**, *26*, 83–90.
5. Huang, X.; Peng, X.; Wang, Y.; Wang, Y.; Shin, D. M.; El-Sayed, M. A.; Nie, S. A Reexamination of Active and Passive Tumor Targeting by Using Rod-Shaped Gold Nanocrystals and Covalently Conjugated Peptide Ligands. *ACS Nano* **2010**, *4*, 5887–5896.
6. Choi, C. H. J.; Alabi, C. A.; Webster, P.; Davis, M. E. Mechanism of Active Targeting in Solid Tumors with Transferrin-Containing Gold Nanoparticles. *Proc. Natl. Acad. Sci. U.S.A.* **2010**, *107*, 1235–1240.
7. Kirpotin, D. B.; Drummond, D. C.; Shao, Y.; Shalaby, M. R.; Hong, K.; Nielsen, U. B.; Marks, J. D.; Benz, C. C.; Park, J. W. Antibody Targeting of Long-Circulating Lipidic Nanoparticles Does Not Increase Tumor Localization but Does Increase Internalization in Animal Models. *Cancer Res.* **2006**, *66*, 6732–6740.
8. Bartlett, D. W.; Su, H.; Hildebrandt, I. J.; Weber, W. A.; Davis, M. E. Impact of Tumor-Specific Targeting on the Biodistribution and Efficacy of siRNA Nanoparticles Measured by Multimodality *In Vivo* Imaging. *Proc. Natl. Acad. Sci. U.S.A.* **2007**, *104*, 15549–15554.
9. Jiang, W.; Kim, B. Y. S.; Rutka, J. T.; Chan, W. C. W. Nanoparticle-Mediated Cellular Response Is Size-Dependent. *Nat. Nanotechnol.* **2008**, *3*, 145–150.
10. Treuel, L.; Brandholt, S.; Maffre, P.; Wiegele, S.; Shang, L.; Nienhaus, G. U. Impact of Protein Modification on the Protein Corona on Nanoparticles and Nanoparticle-Cell Interactions. *ACS Nano* **2014**, *8*, 503–513.
11. Jin, H.; Heller, D. A.; Sharma, R.; Strano, M. S. Size-Dependent Cellular Uptake and Expulsion of Single-Walled Carbon Nanotubes: Single Particle Tracking and a Generic Uptake Model for Nanoparticles. *ACS Nano* **2009**, *3*, 149–158.
12. Walkey, C. D.; Olsen, J. B.; Guo, H.; Emili, A.; Chan, W. C. W. Nanoparticle Size and Surface Chemistry Determine Serum Protein Adsorption and Macrophage Uptake. *J. Am. Chem. Soc.* **2012**, *134*, 2139–2147.
13. Hirn, S.; Semmler-Behnke, M.; Schleh, C.; Wenk, A.; Lipka, J.; Schäffler, M.; Takenaka, S.; Möller, W.; Schmid, G.; Simon, U.; *et al.* Particle Size-Dependent and Surface Charge-Dependent Biodistribution of Gold Nanoparticles after Intravenous Administration. *Eur. J. Pharm. Biopharm.* **2011**, *77*, 407–416.
14. Sonavane, G.; Tomoda, K.; Makino, K. Biodistribution of Colloidal Gold Nanoparticles after Intravenous Administration: Effect of Particle Size. *Colloids Surf., B* **2008**, *66*, 274–280.
15. Choi, C. H. J.; Zuckerman, J. E.; Webster, P.; Davis, M. E. Targeting Kidney Mesangium by Nanoparticles of Defined Size. *Proc. Natl. Acad. Sci. U.S.A.* **2011**, *108*, 6656–6661.
16. Perrault, S. D.; Walkey, C.; Jennings, T.; Fischer, H. C.; Chan, W. C. W. Mediating Tumor Targeting Efficiency of Nanoparticles through Design. *Nano Lett.* **2009**, *9*, 1909–1915.
17. Chou, L. Y. T.; Chan, W. C. W. Fluorescence-Tagged Gold Nanoparticles for Rapidly Characterizing the Size-Dependent Biodistribution in Tumor Models. *Adv. Healthcare Mater.* **2012**, *1*, 714–721.
18. Nam, J.; Won, N.; Bang, J.; Jin, H.; Park, J.; Jung, S.; Jung, S.; Park, Y.; Kim, S. Surface Engineering of Inorganic Nanoparticles for Imaging and Therapy. *Adv. Drug Delivery Rev.* **2013**, *65*, 622–648.
19. Lundqvist, M.; Stigler, J.; Elia, G.; Lynch, I.; Cedervall, T.; Dawson, K. A. Nanoparticle Size and Surface Properties Determine the Protein Corona with Possible Implications for Biological Impacts. *Proc. Natl. Acad. Sci. U.S.A.* **2008**, *105*, 14265–14270.
20. Monopoli, M. P.; Walczyk, D.; Campbell, A.; Elia, G.; Lynch, I.; Bombelli, F. B.; Dawson, K. A. Physical-Chemical Aspects of Protein Corona: Relevance to *In Vitro* and *In Vivo* Biological Impacts of Nanoparticles. *J. Am. Chem. Soc.* **2011**, *133*, 2525–2534.
21. Albanese, A.; Tang, P. S.; Chan, W. C. W. The Effect of Nanoparticle Size, Shape, and Surface Chemistry on Biological Systems. *Annu. Rev. Biomed. Eng.* **2012**, *14*, 1–16.
22. Salvati, A.; Pitek, A. S.; Monopoli, M. P.; Prapainop, K.; Bombelli, F. B.; Hristov, D. R.; Kelly, P. M.; Aberg, C.; Mahon, E.; Dawson, K. A. Transferrin-Functionalized Nanoparticles Lose Their Targeting Capabilities When a Biomolecule Corona Adsorbs on the Surface. *Nat. Nanotechnol.* **2013**, *8*, 137–143.
23. Dai, Q.; Walkey, C.; Chan, W. C. W. Polyethylene Glycol Backfilling Mitigates the Negative Impact of the Protein Corona on Nanoparticle Cell Targeting. *Angew. Chem., Int. Ed.* **2014**, *53*, 5093–5096.
24. De Grand, A. M.; Lomnes, S. J.; Lee, D. S.; Pietrzykowski, M.; Ohnishi, S.; Morgan, T. G.; Gogbashian, A.; Laurence, R. G.; Frangioni, J. V. Tissue-like Phantoms for Near-Infrared Fluorescence Imaging System Assessment and the Training of Surgeons. *J. Biomed. Opt.* **2006**, *11*, 1–21.
25. Kratz, F.; Roth, T.; Fichiner, I.; Schumacher, P.; Fiebig, H. H.; Unger, C. *In Vitro* and *In Vivo* Efficacy of Acid-Sensitive Transferrin and Albumin Doxorubicin Conjugates in a Human Xenograft Panel and in the MDA-MB-435 Mamma Carcinoma Model. *J. Drug Targeting* **2000**, *8*, 305–318.
26. Zhang, S.; Li, J.; Lykotrafitis, G.; Bao, G.; Suresh, S. Size-Dependent Endocytosis of Nanoparticles. *Adv. Mater.* **2009**, *21*, 419–424.
27. Gao, H.; Shi, W.; Freund, L. B. Mechanics of Receptor-Mediated Endocytosis. *Proc. Natl. Acad. Sci. U.S.A.* **2005**, *102*, 9469–9474.
28. Chithrani, B. D.; Chan, W. C. W. Elucidating the Mechanism of Cellular Uptake and Removal of Protein-Coated Gold Nanoparticles of Different Sizes and Shapes. *Nano Lett.* **2007**, *7*, 1542–1550.
29. Jiang, W.; Kim, B. Y. S.; Rutka, J. T.; Chan, W. C. W. Nanoparticle-Mediated Cellular Response Is Size-Dependent. *Nat. Nanotechnol.* **2008**, *3*, 145–150.
30. Adams, G. P.; Schier, R.; McCall, A. M.; Simmons, H. H.; Horak, E. M.; Alpaugh, R. K.; Marks, J. D.; Weiner, L. M. High Affinity Restricts the Localization and Tumor Penetration of Single-Chain Fv Antibody Molecules. *Cancer Res.* **2001**, *61*, 4750–4755.
31. Baxter, L. T.; Jain, R. K. Transport of Fluid and Macromolecules in Tumors. I. Role of Interstitial Pressure and Convection. *Microvasc. Res.* **1989**, *37*, 77–104.
32. Bartlett, D. W.; Davis, M. E. Impact of Tumor-Specific Targeting and Dosing Schedule on Tumor Growth Inhibition after Intravenous Administration of siRNA-Containing. *Nanoparticles* **2008**, *99*, 975–985.
33. Crank, J. *The Mathematics of Diffusion*, 2nd ed.; Oxford University Press: London, 1979.
34. Cabral, H.; Matsumoto, Y.; Mizuno, K.; Chen, Q.; Murakami, M.; Kimura, M.; Terada, Y.; Kano, M. R.; Miyazono, K.; Uesaka, M.; *et al.* Accumulation of Sub-100 nm Polymeric Micelles in Poorly Permeable Tumours Depends on Size. *Nat. Nanotechnol.* **2011**, *6*, 815–823.
35. Wong, C.; Stylianopoulos, T.; Cui, J.; Martin, J.; Chauhan, V. P.; Jiang, W.; Popovic, Z.; Jain, R. K.; Bawendi, M. G.; Fukumura, D. Multistage Nanoparticle Delivery System for Deep Penetration into Tumor Tissue. *Proc. Natl. Acad. Sci. U.S.A.* **2011**, *108*, 2426–2431.
36. Schmidt, M. M.; Wittrup, K. D. A Modeling Analysis of the Effects of Molecular Size and Binding Affinity on Tumor Targeting. *Mol. Cancer Ther.* **2009**, *8*, 2861–2871.
37. Hauck, T. S.; Anderson, R. E.; Fischer, H. C.; Newbigging, S.; Chan, W. C. W. *In Vivo* Quantum Dot Toxicity Assessment. *Small,* **2010**, *6*, 138–144.
38. Fischer, H. C.; Hauck, T. S.; Gómez-Aristizábal, A.; Chan, W. C. W. Exploring Primary Liver Macrophages for Studying Quantum Dot Interactions with Biological Systems. *Adv. Mater.* **2010**, *22*, 2520–2524.
39. Sée, V.; Free, P.; Cesbron, Y.; Nativo, P.; Shaheen, U.; Rigden, D. J.; Spiller, D. G.; Fernig, D. G.; White, M. R. H.; Prior, I. A.; *et al.* Cathepsin L Digestion of Nanobioconjugates upon Endocytosis. *ACS Nano* **2009**, *3*, 2461–2468.
40. Kommareddy, S.; Amiji, M. Biodistribution and Pharmacokinetic Analysis of Long-Circulating Thiolated Gelatin

Nanoparticles Following Systemic Administration in Breast Cancer-Bearing Mice. *J. Pharm. Sci.* **2007**, *96*, 397–407.
41. Dobrovolskaia, M. A.; McNeil, S. E. Immunological Properties of Engineered Nanomaterials. *Nat. Nanotechnol.* **2007**, *2*, 469–478.
42. Perrault, S. D.; Chan, W. C. W. Synthesis and Surface Modification of Highly Monodispersed, Spherical Gold Nanoparticles of 50−200 nm. *J. Am. Chem. Soc.* **2009**, *131*, 17042–17043.
43. Kurfürst, M. M. Detection and Molecular Weight Determination of Polyethylene Glycol-Modified Hirudin by Staining after Sodium Dodecyl Sulfate-Polyacrylamide Gel Electrophoresis. *Anal. Biochem.* **1992**, *200*, 244–248.
44. Gong, X. W.; Wei, D. Z.; He, M. L.; Xiong, Y. C. Discarded Free PEG-Based Assay for Obtaining the Modification Extent of PEGylated Proteins. *Talanta* **2007**, *71*, 381–384.
45. Rydin, R. A.; Deutsch, O. L.; Murray, B. W. The Effect of Geometry on Capillary Wall Dose for Boron Neutron Capture Therapy. *Phys. Med. Biol.* **1976**, *21*, 134–138.
46. Sawyer, S. T.; Krantz, S. B. Transferrin Receptor Number, Synthesis, and Endocytosis during Erythropoietin-Induced Maturation of Friend Virus-Infected Erythroid Cells. *J. Biol. Chem.* **1986**, *261*, 9187–9195.